

# THE STELLAR OBLIQUITY, PLANET MASS, AND VERY LOW ALBEDO OF QATAR-2 FROM K2 PHOTOMETRY

FEI DAI<sup>1</sup>, JOSHUA N. WINN<sup>1,2</sup>, LIANG YU<sup>1</sup>, SIMON ALBRECHT<sup>3</sup>

*Draft version July 16, 2018*

## ABSTRACT

The Qatar-2 transiting exoplanet system was recently observed by the *Kepler* as part of *K2* Campaign 6 in short-cadence mode. We identify dozens of starspot-crossing events, when the planet eclipsed a relatively dark region of the stellar photosphere. The observed patterns of these events demonstrate that the planet always transits over the same range of stellar latitudes, and therefore that the stellar obliquity is less than about  $10^\circ$ . We support this conclusion with two different modeling approaches: one based on explicit identification and timing of the events, and the other based on fitting the light curves with a spotted-star model. We refine the transit parameters and measure the stellar rotation period ( $18.5 \pm 1.9$  days), corresponding to a ‘gyrochronological’ age of  $1.4 \pm 0.3$  Gyr. Coherent flux variations with the same period as the transits are well modeled as the combined effects of ellipsoidal light variations ( $15.4 \pm 4.8$  ppm) and Doppler boosting ( $14.6 \pm 5.1$  ppm). The magnitudes of these effects correspond to a planetary mass of  $2.6 \pm 0.9 M_{\text{Jup}}$  and  $3.9 \pm 1.5 M_{\text{Jup}}$ , respectively. Both of these independent mass estimates agree with the mass determined by the spectroscopic Doppler technique ( $2.487 \pm 0.086 M_{\text{Jup}}$ ). No occultations are detected, giving a  $2\sigma$  upper limit of 0.06 on the planet’s visual geometric albedo. We find no evidence for orbital decay, although we are only able to place a weak lower bound on the relevant tidal quality factor:  $Q'_* > 1.5 \times 10^4$  (95% confidence).

*Subject headings:* planetary systems - planets and satellites: -stars: individual Qatar-2

## 1. INTRODUCTION

The obliquity of a planet-hosting star (the angle between the star’s rotation axis and orbit normal) may bear information about a planet’s formation, migration and tidal evolution history (Queloz et al. 2000; Ohta et al. 2005; Gaudi & Winn 2007; Winn et al. 2010). For example, dynamically hot scenarios for hot Jupiter formation, such as planet-planet scattering (Chatterjee et al. 2008) and Kozai-Lidov mechanism (Fabrycky & Tremaine 2007), should often produce large obliquities. Dynamically cold scenarios such as disk migration (Lin et al. 1996) and *in situ* formation (Batygin et al. 2015) should preserve low obliquities, unless there are mechanisms for exciting obliquities independently of hot-Jupiter formation (e.g., Bate et al. 2010; Batygin 2012).

One way to determine the stellar obliquity — or, to be more precise, to recognize when the obliquity is low — is to observe a sequence of flux anomalies that occur when a transiting planet repeatedly passes in front of a starspot. The analysis of these “starspot-crossing anomalies” takes advantage of the precise time-series photometry that is available for the systems that have been observed by the *Kepler* and *CoRoT* spacecraft. This method does not require intensive time-series spectroscopy, unlike the more traditional method based on the Rossiter-McLaughlin effect, which is often difficult to apply to relatively faint or slowly-rotating stars.

Silva (2003) anticipated the observable signal of a transiting planet crossing over a starspot: the loss of light is temporarily reduced, because the starspot has a lower intensity than the surrounding photosphere. This produces a brief flux enhance-

ment or “bump” in the transit light curve. It soon became clear that spot-crossing anomalies can be used to study the properties of starspots (Silva-Valio et al. 2010), demonstrate the presence of active latitudes (Sanchis-Ojeda & Winn 2011) and constrain the stellar obliquity (Sanchis-Ojeda et al. 2011; Nutzman et al. 2011).

Qatar-2b is a hot Jupiter with a mass of  $2.5 M_{\text{Jup}}$ , a radius of  $1.1 R_{\text{Jup}}$ , and an orbital period of 1.34 days. It was discovered by the Qatar Exoplanet Survey (QES, Bryan et al. 2012). The host star Qatar-2A is a relatively bright K dwarf ( $V = 13.3$ ,  $M_* = 0.740 \pm 0.037 M_\odot$ ). Radial velocity follow-up revealed the presence of a long-term trend which was attributed to a more distant companion. Mancini et al. (2014) constrained the obliquity of Qatar-2b using spot-crossing anomalies seen in the ground-based multi-color transit observations. However, the stellar rotation period was unknown at the time of their analysis. Without the ability to calculate the rotational phase of each transit, Mancini et al. (2014) had to make the assumption that two particular spot-crossing anomalies they observed were caused by eclipses of the same spot. With this assumption, they found the stellar rotation period to be  $14.8 \pm 0.3$  days (after the correction described by Mancini et al. 2016), and the sky-projected obliquity (the angle between the sky projections of the stellar rotation axis and the orbit normal) to be  $\lambda = 4.3 \pm 4.5^\circ$ .

Qatar-2 was within the field of view of *K2* Campaign 6. Being a confirmed planet, Qatar-2 was selected for 1 min (“short-cadence”) time sampling, instead of the usual 30 min sampling. The precise, continuous and well-sampled *K2* photometric data provides an opportunity to study Qatar-2b in greater detail. As we will show, the *K2* data reveal the stellar rotation period to be  $18.5 \pm 1.9$  days, at odds with the period determined by Mancini et al. (2014). Moreover, the *K2* data show evidence for numerous spot-crossing anomalies caused by different spot groups. This leaves little room for doubt in the interpretation of these events, and the conclusion that the

<sup>1</sup> Department of Physics and Kavli Institute for Astrophysics and Space Research, Massachusetts Institute of Technology, Cambridge, MA 02139, USA [fd284@mit.edu](mailto:fd284@mit.edu)

<sup>2</sup> Department of Astrophysical Sciences, Peyton Hall, 4 Ivy Lane, Princeton, NJ 08540 USA

<sup>3</sup> Stellar Astrophysics Centre, Department of Physics and Astronomy, Aarhus University, Ny Munkegade 120, DK-8000 Aarhus C, Denmark

stellar obliquity is low. The short-cadence data also allow for better resolution of the ingress/egress phases of the transit, leading to improved estimates of the basic transit parameters. The data can also be searched for occultations, which would reveal the planet’s dayside brightness; and for ellipsoidal variations (ELV) and the effects of Doppler boosting (DB), the amplitudes of which can be used to make independent estimates of the planetary mass. Finally, the continuous sequence of transit times permits a search for any variations in the intervals between transits, which could be caused by additional orbiting bodies or tidal effects.

The paper is organized in the following way. Section 2 describes our reduction of *K2* data. Section 3 lays out the analysis of the light curve and the refinement of transit parameters. Section 4 presents a search for changes in the transit period. Section 5 discusses the measurement of the stellar rotation period, and the associated “gyrochronological” age. Section 6 presents the search for occultations, ELV, and DB effects. Section 7 presents the analysis of spot-crossing anomalies and the implications for the stellar obliquity. Finally, Section 8 summarizes and discusses all our findings.

While this work was in the final stages of preparation, we became aware of the work of Močnik et al. (2016), who performed a similar analysis of the same data. Our study and their study have reached similar conclusions regarding the stellar obliquity, stellar rotation period, transit-timing results, and flux modulation outside of transits. Some small differences exist in the quantitative results, which we describe in the appropriate sections.

## 2. K2 PHOTOMETRY

Qatar-2 (or EPIC 212756297) was observed during *K2* Campaign 6 from 2015 Jul 11 to Oct 3 in the short-cadence mode. We downloaded the pixel files from Mikulski Archive for Space Telescopes (MAST) website. As is now well known, the photometric precision of *K2* data is not as good as the original *Kepler* mission, due to the uncontrolled rolling motion around the telescope’s boresight combined with the inter-pixel and intra-pixel sensitivity variations (Howell et al. 2014). To produce a photometric time series from the pixel-level data, we used an approach similar to that described by Vanderburg & Johnson (2014). In short, we used a circular aperture of 4.5 pixels in radius centered around the brightest pixel. To determine the flux-weighted center of light, we fitted a two-dimensional Gaussian function to the flux distribution of the pixels within this aperture. We then fitted a piecewise linear function between the aperture-summed flux and the coordinates of the center of light, and used the parameters of the best-fitting function to correct the aperture-summed flux time series. Fig. 1 shows the corrected time series.

## 3. REFINING TRANSIT PARAMETERS

The high precision and high temporal sampling rate provided by *K2* short-cadence observations are ideal for resolving the ingress and egress phases of the transit, as well as revealing any anomalies in the transit profile. Before searching for anomalies, we used the short-cadence light curve to refine the basic transit parameters of Qatar-2b. Because the extant radial-velocity data are consistent with a circular orbit (Bryan et al. 2012), we assumed the orbit to be circular orbit in all our analyses.<sup>4</sup>

<sup>4</sup> The orbital eccentricity can also be constrained from the timing of the secondary eclipse; however, we did not detect the signal of the secondary eclipse in the *K2* data (see Section 6).

We started with the corrected *K2* light curve (Fig. 1) and published transit parameters (Bryan et al. 2012). We first analyzed each transit individually by isolating a 7-hour window around the expected mid-transit times. To remove the long-term stellar variability, we allowed the flux baseline to be a quadratic function of time, in addition to modeling the loss of light due to the planetary transits. For the transit model, we used the Python package *Batman* by Kreidberg (2015). We adopted a quadratic limb-darkening profile. We chose not to impose any priors on the two limb-darkening coefficients because the short-cadence data proved to provide adequate constraints on both coefficients (see Table 1).

Another effect that alters the transit profile is the presence of starspots outside of the transit chord. Transit models such as *Batman* assume the photosphere to be unspotted. When spots are present, the untransited portion of the photosphere makes a smaller relative contribution to the total flux than is assumed in the model. If this is not accounted for, the model parameters would compensate for the relatively large loss of light by increasing the planet size, giving a biased result. To account for this effect, we introduced an additional parameter specific to each transit:  $\Delta F_{\text{spot}}$ , the relative loss of light due to any unocculted spots on the visible hemisphere. The calculated flux that is compared to the observed flux is

$$F_{\text{calc, spot}} = \frac{F_{\text{calc, no-spot}} - \Delta F_{\text{spot}}}{1 - \Delta F_{\text{spot}}} \quad (1)$$

where  $F_{\text{calc, spot}}$  and  $F_{\text{calc, no-spot}}$  are respectively the theoretical flux with and without taking the unocculted starspots into account. In this equation, the role of the denominator is to ensure that  $F_{\text{calc, spot}} \equiv 1$  outside of the transits, since the data have been normalized in this manner.

In summary, the set of parameters describing each transit are the time of inferior conjunction ( $T_c$ ); the three parameters of the quadratic function of time representing stellar variability ( $a_2$ ,  $a_1$ , and  $a_0$ ); and the loss of light due to unocculted spots on the visible hemisphere ( $\Delta F_{\text{spot}}$ ). There are also the usual transit parameters: the planet-to-star radius ratio ( $R_p/R_*$ ); the ratio of stellar radius to orbital distance ( $R_*/a$ ); the impact parameter ( $b$ ), and the limb-darkening coefficients ( $u_1$  and  $u_2$ ). We adopted the usual  $\chi^2$  likelihood function and found the maximum-likelihood solution using the Levenberg-Marquardt algorithm as implemented in the Python package *lmfit* (Newville et al. 2014).

Spot-crossing anomalies are clearly visible in the time series of residual fluxes. Fig. 7 shows some examples. These anomalies would be a source of bias in the model parameters, if no corrections were performed. We identified these anomalies through visual inspection, and modeled them as Gaussian functions of time:

$$F_{\text{anom}}(t) = A \exp \left[ -\frac{(t - t_{\text{anom}})^2}{2\sigma_{\text{anom}}^2} \right] \quad (2)$$

where  $A$ ,  $t_{\text{anom}}$  and  $\sigma_{\text{anom}}$  represent (respectively) the amplitude, time, and duration of the anomaly.

In some cases, visual inspection of a given transit revealed more than one spot-crossing anomaly. To decide on the number of spot-crossing anomalies to include in the final model, we fitted the light curve with increasing numbers of spots, and calculated the change in the Bayesian Information Criterion,

$$\text{BIC} = 2\log(L_{\text{max}}) + N \log(M), \quad (3)$$

where  $L_{\text{max}}$  is the maximum likelihood,  $N$  is the number of

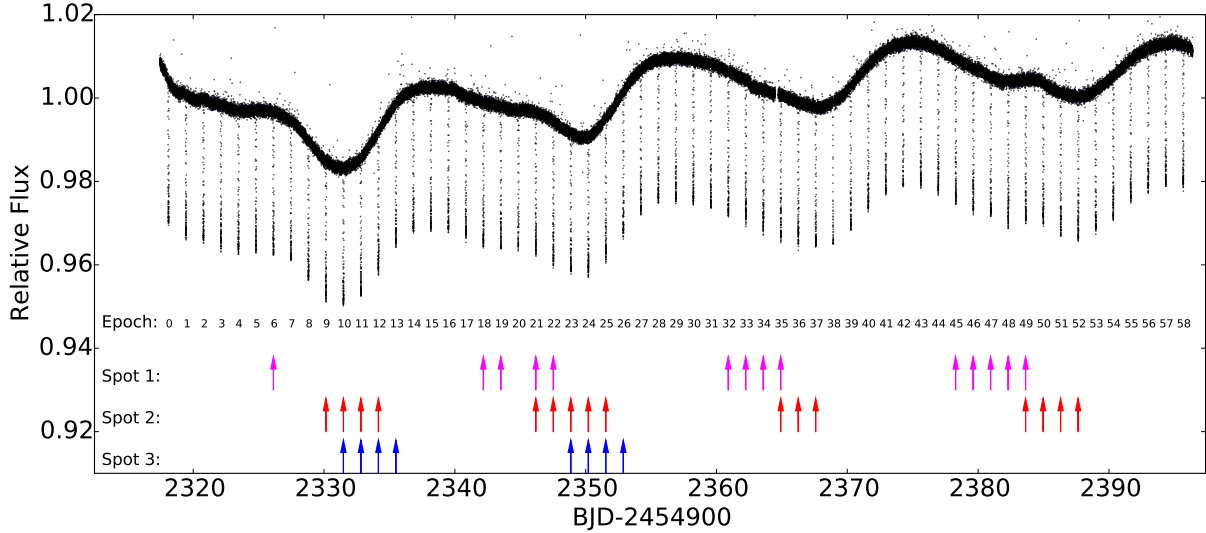


FIG. 1.— Corrected K2 photometry of Qatar-2. Colored arrows indicate the times of identified spot-crossing anomalies (see Table 4 for the full list of anomalies and Section 7.1 for how the anomalies were grouped). Anomalies recur in groups of  $\approx 4$ , on a timescale similar to the stellar rotation period of  $\approx 18$  days.

model parameters, and  $M$  is the number of data points. We only retained those anomalies for which  $\Delta\text{BIC} > 10$ . Table 4 reports the properties of all these anomalies. The parameter uncertainties were determined via the Markov Chain Monte Carlo (MCMC) method, as implemented in the Python package `emcee` (Foreman-Mackey et al. 2013). Here and elsewhere in this paper, the reported parameter value is based on the 50% level of the cumulative posterior distribution, and the uncertainty interval is based on the 16% and 84% levels.

We used the best-fitting parameters to correct the data from each transit for stellar variability and unocculted spots. We also removed the spot-crossing anomalies by excluding data points within  $2\sigma_{\text{anom}}$  of the time of each anomaly. We combined all 59 of the rectified and spot-cleaned transit intervals to create a phase-folded transit light curve with a very high signal-to-noise ratio. Then we modeled this phase-folded light curve to determine the basic transit parameters, using another MCMC analysis (see Fig. 2).

We then assumed that these basic transit parameters are fixed in time and applicable to each and every transit. We repeated the analyses of all of the individual transits, holding the transit parameters fixed at the values determined from the analysis of the phase-folded light curve. This in turn allowed the creation of a new version of the phase-folded light curve. After two such iterations it was clear that the results had already converged. Table 1 gives the results.

#### 4. LACK OF TRANSIT TIMING VARIATIONS

To search for evidence of any changes in the orbital period since the time of discovery of Qatar-2b, we combined our measured midtransit times with those found on the Exoplanet Transit Database (ETD) website. Table 2 gives all the midtransit times in the Barycentric Dynamical Time system (Eastman et al. 2010,  $\text{BJD}_{\text{TDB}}$ ).

Fig. 3 shows the residuals between the observed times and the calculated times according to the best-fitting constant-period model. The only obvious pattern in the residuals is that the data points from the second season are generally above the baseline, while the third season’s data are below the baseline. It will be interesting to see if these long-term variations are

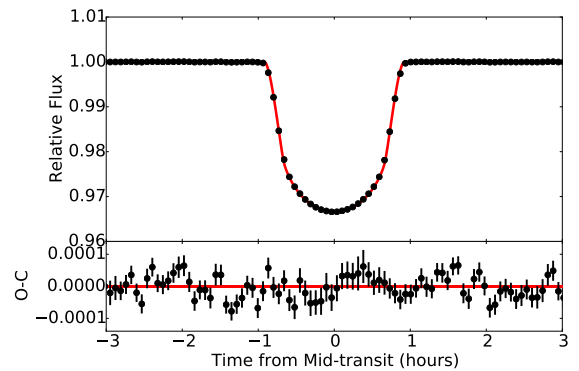


FIG. 2.— *Top*.—Phase-folded transit light curve of Qatar-2, after correcting for stellar variability, unocculted spots, and spot-crossing anomalies. The red line shows the best-fitting model. The data have been averaged in phase within intervals of 3 minutes. *Bottom*.—Residuals between the data and the best-fitting model.

seen in future seasons. We do not find any sinusoidal-like variations that are sometimes seen in multi-planet systems. We computed the Lomb-Scargle periodogram (Lomb 1976; Scargle 1982) of the timing residuals; no signal was detected with a false alarm probability less than 10%. We also did not detect any evidence for a secular change in the orbital period, as described below. The lack of detectable period shrinkage allows us to place a constraint on the rate of tidal dissipation in the system. Tidal evolution is expected to cause period decay with a rate that scales as  $(M_p/M_*)(R_*/a)^5$  (Levrard et al. 2009), which is relatively large for this system because of the close-in orbit. For quantitative constraints on the rate, we fitted the following function to the sequence  $T_n$  of midtransit times:

$$T_n = T_0 + nP_0 + \frac{1}{2}n^2 \frac{dP}{dn}. \quad (4)$$

We conducted a MCMC analysis using `emcee` and the usual  $\chi^2$  likelihood function, and uniform priors for all parameters. The result for the period-change parameter was an upper limit,

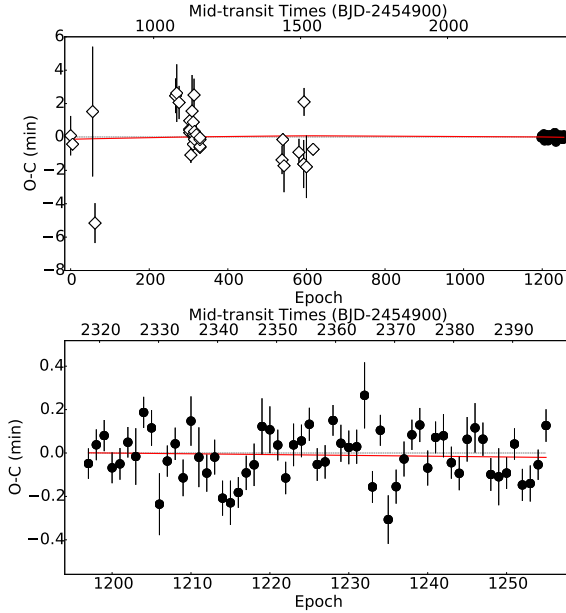


FIG. 3.— Observed minus calculated transit times of Qatar-2b, where the calculated times are based on the best-fitting constant-period model. The top panel shows all the available data, and the bottom panel allows a closer view of the *K2* data. Table 2 gives the numerical data.

$|\frac{dP}{dN}| < 0.11$  milliseconds, or  $|\frac{dP}{dt}| < 1.7 \times 10^{-9}$  (95% conf.). To translate these upper bounds into a lower bound on the stellar tidal quality factor we used the formula (Levrard et al. 2009)

$$Q'_* = 9P^2 \left( \frac{dP}{dN} \right)^{-1} \frac{M_p}{M_*} \left( \frac{R_*}{a} \right)^5 \left( \omega_* - \frac{2\pi}{P} \right), \quad (5)$$

where  $\omega_*$  is the angular velocity of stellar rotation. The derivation of this formula assumes a circular orbit and zero obliquity. For Qatar-2, a low eccentricity is compatible with the available radial velocity dataset (Bryan et al. 2012), and a low obliquity is implied by our analysis in Section 7. The result of applying this formula to our data is  $Q'_* > 1.5 \times 10^4$  (95% conf.).

## 5. STELLAR ROTATION PERIOD AND GYROCHRONOLOGY

The *K2* light curve (Fig. 1) exhibits quasiperiodic flux variations with four cycles. These variations are characteristic of starspots being carried around by rotation, and therefore the stellar rotation period can be estimated from the period of these flux variations. For a quantitative estimate, we masked out the transits and calculated the Lomb-Scargle periodogram (Lomb 1976; Scargle 1982) of the resulting time series, which is shown in Fig. 4. Based on the location and width of the most prominent peak in the periodogram, we estimate the stellar rotation period to be  $18.5 \pm 1.9$  days.

Knowledge of the stellar rotation period played a crucial role in our obliquity determination (see Section 7). In addition, for main-sequence stars such as Qatar-2, the rotation period is linked to the stellar age, a relationship that has come to be known as "gyrochronology." We estimated the age of the system using a gyrochronological formula that was derived by

Schlaufman (2010):

$$P_*(M_*, \tau_*) = P_{*,0}(M_*) \left( \frac{\tau_*}{650 \text{ Myr}} \right)^{1/2}, \quad (6)$$

where  $P_*(M_*, \tau_*)$  is the rotation period of a star with mass  $M_*$  and age  $\tau_*$ , and  $P_{*,0}(M_*)$  is a specified polynomial function that was calibrated using data from the Hyades and Praesepe star clusters. Using this formula and our measured rotation period, the gyrochronological age of Qatar-2 is  $1.4 \pm 0.3$  Gyr.

Maxted et al. (2015) made an independent estimate of the stellar age by fitting stellar-evolutionary models to the observed spectroscopic parameters and apparent magnitudes. Their result was  $15.7 \pm 1.4$  Gyr, significantly older than the gyro age. Assuming this older age is correct, the younger gyro age could be taken as evidence that the star has been spun up by the tidal torque of the close-in planet. However, Maxted et al. (2015) expressed concern that their estimate is unrealistic because their method may be biased by the "inflated K-dwarf" phenomenon, a known problem with stellar-evolutionary models in fitting the observed properties of stars similar to Qatar-2.

Močnik et al. (2016) also used *K2* data to determine the stellar rotation period, and found the gyro age to be  $0.59 \pm 0.10$  Gyr. This is significantly younger than our estimate of the gyro age. Since their result for the rotation period was essentially equivalent to ours, the difference in gyro ages must be attributable to the different gyrochronological formula that was adopted by Močnik et al. (2016). They used a formula presented by Barnes (2007), while we used the formula above from Schlaufman (2010). Evidently the gyro age is subject to a systematic uncertainty that is more important than the uncertainty in the stellar rotation period.

Another use for the stellar rotation period is to estimate the inclination  $i_*$  between the stellar rotation axis and the line of sight. This is done through the following formula:

$$\sin i_* = \frac{v \sin i_*}{v} = \frac{v \sin i_*}{2\pi R_* / P_{\text{rot}}}, \quad (7)$$

where  $v \sin i_*$  is the projected rotation rate that can be estimated from the degree of rotational broadening that is observed in the star's photospheric absorption lines. For Qatar-2, Bryan et al. (2012) found  $v \sin i_* = 2.8 \pm 0.5 \text{ km s}^{-1}$ , while our results lead to  $v = 2\pi R_* / P_{\text{rot}} = 2.0 \pm 0.3 \text{ km s}^{-1}$ , giving  $\sin i_* = 1.4 \pm 0.6$ . This is compatible with unity, as expected for a low-obliquity star, although the uncertainty is large enough to encompass inclinations as low as  $50^\circ$  (as well as mathematically impossible values of  $\sin i_*$ ).

## 6. PHASE CURVE ANALYSIS AND SECONDARY ECLIPSE

Thanks to the high precision and nearly continuous temporal coverage of the *K2* data, we may perform a sensitive search for the occultation of Qatar-2b by its parent star (the secondary eclipse), as well as out-of-eclipse light variations associated with the orbital period. The latter type of variations could arise from the tidally-induced ellipsoidal figure of the star (ELV), Doppler boosting (DB), and illumination effects (ILL), as exemplified by Mazeh & Faigler (2010). All of these effects are expected to be small, on the order of  $\sim 10$  ppm. Thus it is difficult, and important, to try and distinguish any residual systematic effects in the time series from the astrophysical effects.

For this reason we performed all our analyses on several versions of the *K2* light curve, all of which used different

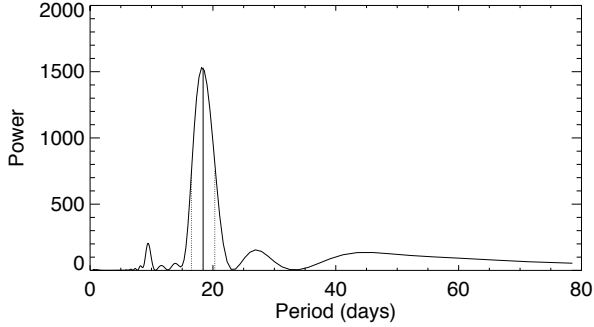


FIG. 4.— Lomb-Scargle periodogram of the out-of-transit flux variations of Qatar-2. Based on the location and width of the most prominent peak we estimate the rotation period to be  $18.5 \pm 1.9$  days.

algorithms to try and filter out systematic effects and artifacts. Specifically we used the versions known as *K2SFF* (Vanderburg & Johnson 2014; Vanderburg et al. 2016), *K2SC* (Aigrain et al. 2016; Pope et al. 2016), *K2 Everest* (Luger et al. 2016), and our own processed light curve. We found that while all of the light curves gave consistent results, *K2 Everest* seemed to have the lowest levels of residual systematic trends and artifacts. This particular algorithm differs from all the others by being based on Pixel Level Decorrelation (Deming et al. 2015, PLD). All the other methods rely on measurements of the flux-weighted center of light of a specified collection of pixels. The results described in the rest of this section are based on the *K2 Everest* light curve.

We omitted all the data within 3 hours of each midtransit time. To remove the long-term stellar variability, we divided the light curve by a cubic spline with a temporal width of twice the orbital period. We then folded the time series with the orbital period of the planet, and averaged the resulting light curve into 100 bins equally spaced in orbital phase. We fitted for the ELV, DB and ILL effects simultaneously (See Fig. 5). For the ILL component, we adopted a Lambertian phase function. The combined model for the variations took the form

$$F_0 - A_{\text{ELV}} \cos(4\pi\phi) + A_{\text{DB}} \sin(2\pi\phi) + A_{\text{ILL}} \frac{\sin(z) + (\pi - z)\cos(z)}{\pi} \quad (8)$$

where

$$\cos(z) = -\sin(i)\cos(2\pi\phi + \theta) \quad (9)$$

and

$$\phi = \frac{t - T_c}{P}. \quad (10)$$

In these equations,  $F_0$  is an additive constant,  $A_{\text{ELV}}$ ,  $A_{\text{DB}}$  and  $A_{\text{ILL}}$  are the amplitudes of the ELV, DB and ILL effects,  $T_c$  is the time of inferior conjunction,  $P$  is the orbital period,  $i$  is the orbital inclination, and  $\theta$  represents a hypothetical offset between the maximum of the phase curve and the time of superior conjunction. We also fitted for the loss of light during the secondary eclipse, using *Batman*, and requiring the depth of the secondary eclipse to be consistent with  $A_{\text{ILL}}$ . Initially, we allowed the phase of the secondary eclipse to be a free parameter; once it became clear that no secondary eclipse could be detected, we reverted to the assumption of a circular orbit and thereby required the secondary eclipse to occur at  $\phi = 0.5$ .

We conducted an MCMC analysis with *emcee*, with uniform priors on all the parameters. The  $A_{\text{ELV}}$  and  $A_{\text{DB}}$  param-

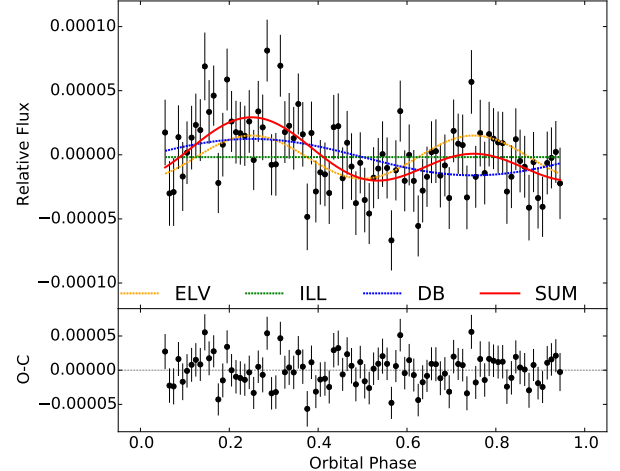


FIG. 5.— The phase-folded and binned light curve of Qatar-2, after excluding the transits and filtering as described in the text. The red curve shows the best-fitting model. The different components of the model are shown in different colors (except the additive constant, which is not shown.) No secondary eclipse was detected.

eters were both found to be nonzero. Specifically,  $A_{\text{ELV}} = 15.4 \pm 4.8$  ppm and  $A_{\text{DB}} = 14.6 \pm 5.1$  ppm. Both of these effects depend on the planet mass, along with additional system parameters that are largely constrained by other observations. Therefore we may use the results for  $A_{\text{ELV}}$  and  $A_{\text{DB}}$  to make independent determinations of the planet mass. For this purpose we used Equations (11), (12) and (15) of Carter et al. (2011). The mass implied by the ELV amplitude is  $M_{p, \text{ELV}} = 2.6 \pm 0.9 M_{\text{Jup}}$ , while the mass implied by the DB amplitude is less certain  $M_{p, \text{DB}} = 3.9 \pm 1.5 M_{\text{Jup}}$ . These two independent estimates are consistent with each other to within one sigma, and also agree with the mass determination  $M_{p, \text{RV}} = 2.487 \pm 0.086 M_{\text{Jup}}$  based on the more secure and traditional Doppler technique (Bryan et al. 2012). This lends confidence to our assessment that the out-of-transit flux variations are astrophysical rather than being dominated by instrumental or systematic effects.

Neither the ILL effect nor the secondary eclipse were detected. The resulting upper bound on  $A_{\text{ILL}}$  is 35 ppm (95% conf.). This represents an upper bound on the combination of the planet’s reflected light and thermal emission. Assuming that the thermal emission is negligible within the *Kepler* bandpass, the resulting upper limit on the planet’s geometric albedo is  $A_g < 0.06$ . Any contribution from thermal emission would require an even smaller geometric albedo. Conversely, if the reflected component is assumed to be negligible we may place an upper bound on the effective temperature of the planet, after making the simplifying assumption that the planet emits as a blackbody. The resulting upper limit is  $T_{\text{eff}} < 1500$  K (95% conf.). This is consistent with the calculated equilibrium temperature of  $T_{\text{eq}} \approx 1300$  K, assuming a Bond albedo of zero.

## 7. SPOT-CROSSING ANOMALIES AND OBLIQUITY MEASUREMENT

In this section, we present the analysis of the spot-crossing anomalies. The patterns of recurrence of the spot-crossing anomalies implies that the transit chord is aligned with the lines of latitude on the star, which in turn implies that the star has a low obliquity. For quantitative analysis we employed



two different approaches, each of which has its advantages and limitations.

### 7.1. Anomaly identification and timing

First we employed a simple geometric model for which the parameters are constrained by the measured times of spot-crossing anomalies. Similar models have previously been used to constrain the obliquity of planet-hosting stars (Sanchis-Ojeda et al. 2011; Nutzman et al. 2011). The premise is straightforward: when an anomaly is observed, the planet’s position on the sky must at least partially overlap the location of the starspot. We define our coordinate system in the plane of sky such that the  $x$ -axis is aligned with the line of nodes of the planetary orbit, and the  $y$ -axis is in the perpendicular direction. Using the basic transit parameters determined earlier, we calculate the projected  $x$  and  $y$  coordinates of the planet as a function of time. We choose a particular spot-crossing anomaly as the nominal starting point, at which the starspot is placed at the position of the planet. Then we can predict any future or past location of the starspot, given the following parameters: the stellar inclination ( $i_*$ ), the sky-projected obliquity ( $\lambda$ ), the stellar rotation period ( $P_{\text{rot}}$ ), and the stellar latitude of the spot ( $l$ ). For simplicity we assume that the starspot does not change significantly in size, intensity, or location during the interval over which the model is applied. This assumption is more valid when focusing on a relatively short time interval.

Fig. 6 illustrates this model, using the anomalies associated with Spot 3 in Table 4. The black dots show the calculated positions of the planet during each spot-crossing anomaly caused by Spot 3. We initialized the model by assuming that the spot and planet coincided at the time of the first anomaly (Epoch 10, red circle). The blue curve shows the spot’s trajectory on the stellar photosphere, and the blue triangles show the calculated positions of the spot at the times of the observed anomalies. The success of the model is indicated by the close coincidence between the positions of the planet and spot.

A key question is what to do when there are multiple spots on the star, which is likely in general, and definitely the case for Qatar-2. When the model has multiple spots, how do we associate individual spot-crossing anomalies with a particular spot? First we grouped the spot-crossing anomalies into families through visual inspection of their relative phases, amplitudes and durations. We then revised these assignments as needed when the model revealed significant outliers indicating a mistaken association. Our final assignments are justified by noting that the analysis of all the different groups were consistent with the same rotation period, which is in turn consistent with the rotation period estimated from the *K2* light curve (see Table 5).

Although this procedure seems to work, the necessity to group the anomalies as we have just described is a shortcoming of this simple geometric model. This weakness is especially acute when the technique is applied to ground-based data, for which quasi-continuous monitoring is very difficult to achieve. As an example, Mancini et al. (2014) did not have the stellar rotation period as an independent check for their model of Qatar-2b. By assuming that two particular spot-crossing anomalies they observed were associated with a single spot, they derived a stellar rotation period of  $14.8 \pm 0.3$  days (as later revised by Mancini et al. 2016). This is now known to be incorrect; most likely, the two observed anomalies were produced by crossings over two different spots.

For quantitative constraints on the obliquity, we adopted the

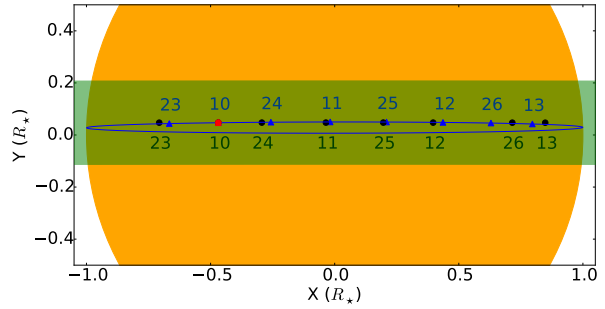


FIG. 6.— Illustration of the first modeling approach, in which we measure the times of anomalies that seem associated with a single spot, and constrain a geometric model by requiring the planet and spot to be nearly coincident on the sky plane at those times. The orange circle represents the stellar disk. The green band is the transit chord. The black circles are the calculated positions of the planet during each spot-crossing anomaly that was assigned to Spot 3 from Table 4. The numbers specify the transit epoch numbers. The blue curve is the calculated trajectory of Spot 3, and the blue triangles are the calculated locations of Spot 3 at the time of the anomalies. The success of the model is illustrated by the near-coincidence of the planet and spot at the times of all the anomalies.

likelihood function

$$L = \exp(-\chi^2/2), \quad (11)$$

where

$$\chi^2 = \sum_i^{N_{\text{anom}}} \frac{(x_{\text{spot},i} - x_{\text{planet},i})^2 + (y_{\text{spot},i} - y_{\text{planet},i})^2}{(0.5 R_p)^2} + \text{NDP}. \quad (12)$$

Here,  $N_{\text{anom}}$  is the number of spot-crossing anomalies; and  $x_{\text{spot},i}$ ,  $y_{\text{spot},i}$ ,  $x_{\text{planet},i}$  and  $y_{\text{planet},i}$  are the coordinates of the spot and the planet at the time of the  $i$ th anomaly. With this function, we reward models that place the planet and spot close to one another at the times of observed anomalies. By choosing the length scale to be  $0.5 R_p$  we have assumed that the spot sizes are comparable to the size of the planet, or smaller. The NDP term is the non-detection penalty, which adds 100 to  $\chi^2$  if there is no observed anomaly at a time when the model predicts one. We acknowledge that the choice of length scale and NDP are *ad hoc*, preventing the quantitative results from being taken too seriously; the purpose of the modeling is simply to demonstrate that low-obliquity solutions are able to account for the most prominent sequences of anomalies.

To begin, we identified the three most prominent series of spot-crossing anomalies (labeled with red, blue, and magenta arrows in Fig. 1), and analyzed each one of these families separately with a one-spot model. Then after being satisfied that they gave consistent results, we performed a joint analysis of all the spot-crossing anomalies using a three-spot model. Table 5 gives all the results, based on an MCMC analysis. We reiterate that the quantitative results are contingent on the choices of length scale and NDP in the likelihood function, which were chosen somewhat subjectively. The main point is that in all cases, the sky-projected obliquity is consistent with zero, and the stellar rotation period is consistent with the independently measured period of  $18.5 \pm 1.9$  days. The stellar inclination  $i_*$  and spot latitude  $l$  are only loosely constrained, and their uncertainties are strongly correlated, demonstrating another limitation of this modeling approach.

### 7.2. Light-curve fitting

As a second approach to demonstrate the low obliquity of Qatar-2, we constructed a numerical model for the loss of light due to a planetary transit over a star with circular starspots. We used a two-dimensional Cartesian grid to represent the stellar disk, and assigned intensities to the pixels based on the assumed limb-darkening law and the locations of starspots and the planet (see Fig. 8). For simplicity the spots were assumed to be circular and uniform in intensity, with unchanging properties and locations in the rotating frame of the star. Thus, in addition to the usual transit parameters, this model has parameters for the spot's angular size ( $\alpha$ ), intensity contrast ( $f$ ), latitude ( $l$ ), and the time ( $t$ ) when it crosses the  $x$ -axis. We also allow each spot to be associated with an independent rotation period,  $P_{\text{rot},i}$ , to allow for a consistency check (and to allow for a modest degree of differential rotation, although we did not end up finding evidence for this effect).

At any particular time, we located the pixels affected by the spot by taking the dot product between the surface normal associated with the pixel and the position vector of the spot. The intensity of any pixel within the angular radius of a spot center was multiplied by the spot's contrast factor. The pixels within the planet's silhouette were assigned zero intensity. Then the summed intensity of all the pixels was compared to the observed flux, and the usual  $\chi^2$  statistic was calculated. We held fixed the transit parameters at the best-fitting values obtained in Section 3.

The pixelated model is conceptually straightforward, but it requires two-dimensional integration, which is computationally expensive. Béky et al. (2014) wrote a semi-analytic code called `Spotrod` to model spot-crossing anomalies, also assuming uniform and circular spots. Their algorithm is more computationally efficient because the integration is reduced to one dimension through the analytic calculation of the points of intersection between the spot and planet. We analyzed the light curve with our own 2-d model as well as `Spotrod`, to check for consistency.

Although more than half of the transits observed by *K2* showed evidence for spot-crossing anomalies, we chose to model five consecutive anomalies with the highest signal-to-noise ratio. We chose to limit the time interval of the model to  $\approx 5$  days because we are not modeling spot evolution.

First we found the maximum likelihood model, using the Levenberg-Marquardt algorithm as implemented in `lmfit`. We then conducted a MCMC analysis with `emcee`. Table 6 gives the results. The results from our 2-d numerical model and `Spotrod` are very similar. The stellar inclination was found to be within about  $10^\circ$  of edge-on, and the sky-projected obliquity was found to be consistent with zero within about  $5^\circ$ . The stellar rotation period was found to agree well with the value reported previously in Section 5. The angular radius of the spot was around  $10^\circ$ , much larger than sunspots.

The numerical light-curve modeling may appear to offer very precise constraints on the obliquity and other system parameters. However, just as was the case with our first modeling approach, the precise quantitative results should not be taken too seriously. In this case it is because the light curve models make strong assumptions about the shape and intensity distribution of the spots, as well as the lack of any spot migration or evolution. There is no reason to believe that the spots are circular, and indeed each "spot" may in reality be a complex, splotchy arrangement of spots and plages. We re-

gard the numerical results as a conceptually straightforward demonstration that the obliquity is likely to be smaller than about  $10^\circ$ .

## 8. SUMMARY AND DISCUSSION

In this work, we presented the analysis of the *K2* short-cadence observation of Qatar-2. The continuous monitoring, high precision and high cadence of the *K2* data helped to refine the transit parameters. In addition, the data quality was high enough to facilitate the identification and exclusion of data points affected by spot-crossing anomalies, leading to a less biased set of transit parameters.

We measured the stellar rotation period of Qatar-2A  $18.5 \pm 1.9$  days based on the out-of-transit flux variation of the *K2* light curve. Using the technique of gyrochronology, the rotation period led to an independent estimate of the stellar age,  $1.4 \pm 0.3$  Gyr. The rotation period also played a crucial role in our obliquity determination; the lack of an independently measured rotation period had been a missing piece of the puzzle in a previous effort to determine the stellar obliquity.

The nondetection of the secondary eclipse allowed us to place a constraint on the planet's geometric albedo in the *Kepler* bandpass:  $A_g < 0.06$ , with 95% confidence. This is consistent with previous investigations that showed "hot Jupiters" often have low albedos (Esteves et al. 2015; Gandolfi et al. 2013; Kipping & Spiegel 2011).

We detected the ellipsoidal light variation and Doppler boosting effects in the *K2* light curve, after filtering out long-term stellar variability and systematic effects. The magnitudes of these two effects imply planetary masses of  $2.6 \pm 0.9 M_{\text{Jup}}$  and  $3.9 \pm 1.5 M_{\text{Jup}}$ , both of which are consistent with the mass determined from the spectroscopic Doppler technique (Bryan et al. 2012). We have updated the ephemerides of Qatar-2b with the new mid-transit times observed by *K2*. There is no evidence for orbital decay, leading to a lower bound on the stellar tidal quality factor  $Q'_* > 1.5 \times 10^4$  (95% confidence).

We identified dozens of spot-crossing anomalies in the *K2* light curve. These anomalies revealed the presence of active regions on the host star along the planet's transit chord. This suggests that Qatar-2 is magnetically active, as one would expect for a star with the relatively young age that was determined from gyrochronology. We used the observed spot-crossing anomalies to demonstrate that the obliquity of Qatar-2 is very likely smaller than  $10^\circ$ . We did this in two different ways. First we identified individual spot-crossing anomalies and measured their properties, including their times of occurrence. We then used a simple geometric model for which the parameters were determined by requiring spatial coincidences of the spot and the planet at the times of observed anomalies. In a separate approach, we fitted a photometric model to a portion of the light curve, based on the premise of a planet transiting a limb-darkened star with a circular starspot.

Neither model can be relied upon for precise quantitative results, because of the strong assumptions that were made, such as the circular shape of the spots and the lack of spot evolution. Nevertheless the qualitative results leave little room for doubt that the obliquity is lower than  $10^\circ$ . A low obliquity for Qatar-2 is consistent with a pattern that has been previously noted: the hot Jupiter hosts with photospheres cooler than about 6100-6300 K tend to have low obliquities (Winn et al. 2010).

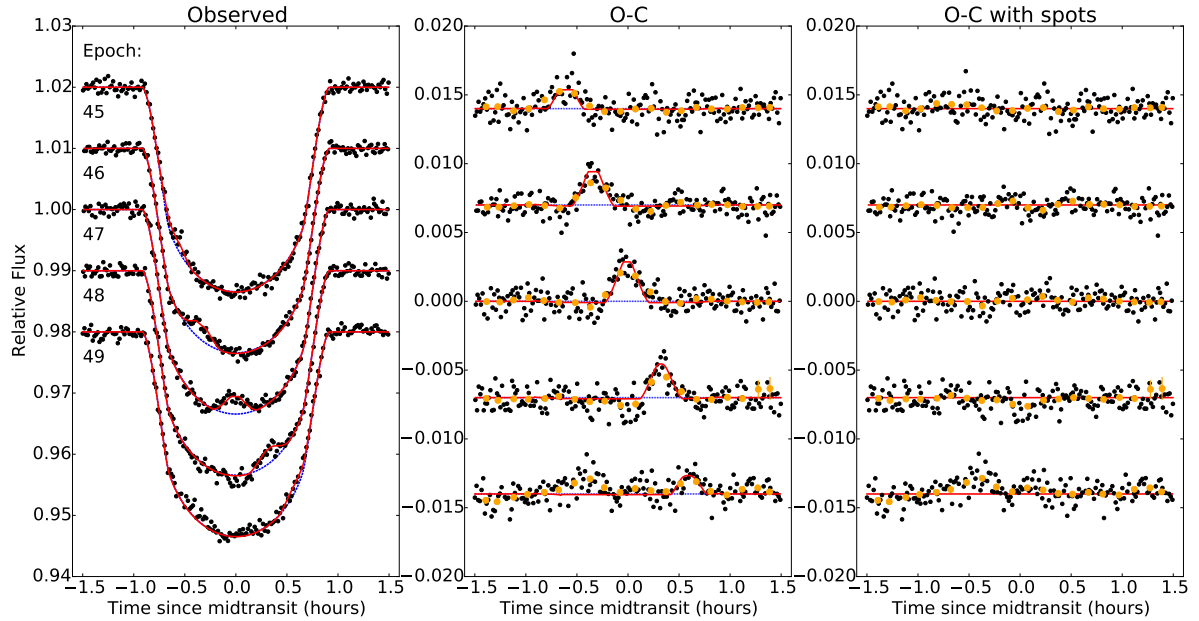


FIG. 7.— *Left*.—The five consecutive transit light curves that were selected for detailed modeling. Arbitrary vertical offsets have been applied to data from different epochs. The dotted blue line is the best-fitting model with no spots. The solid red line is the best-fitting single-spot model. *Middle*.—Residuals, after subtracting the no-spot model. The spot-crossing anomalies are seen to progress steadily in phase from one transit to the next, at the rate that is expected, based on the orbital period and the stellar rotation period. *Right*.—Residuals, after subtracting the single-spot model.

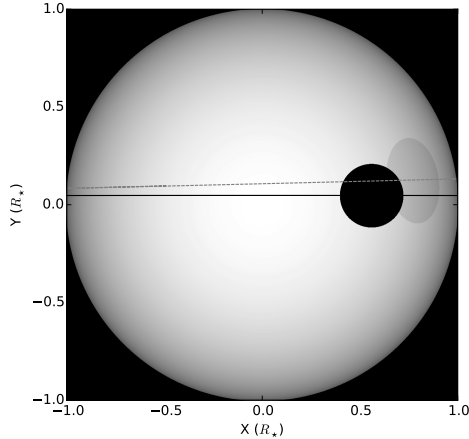


FIG. 8.— Illustration of the best-fitting spot model from Fig. 7, at the time of Epoch 49. Visible are the limb-darkened photosphere, the starspot (light gray ellipse near the limb), and the planet (black circle). The dashed line is the spot's trajectory across the stellar disk, and the solid line is the planet's trajectory. A given spot produces a smaller anomalies when it is projected near the limb, due to geometrical foreshortening and limb-darkening.

#### REFERENCES

- Aigrain, S., Parviainen, H., & Pope, B. J. S. 2016, *MNRAS*, 459, 2408  
 Barnes, S. A. 2007, *The Astrophysical Journal*, 669, 1167  
 Bate, M. R., Lodato, G., & Pringle, J. E. 2010, *MNRAS*, 401, 1505  
 Batygin, K. 2012, *Nature*, 491, 418  
 Batygin, K., Bodenheimer, P. H., & Laughlin, G. P. 2015, *ArXiv e-prints*, arXiv:1511.09157  
 Béky, B., Kipping, D. M., & Holman, M. J. 2014, *MNRAS*, 442, 3686  
 Bryan, M. L., Alsubai, K. A., Latham, D. W., et al. 2012, *ApJ*, 750, 84  
 Carter, J. A., Rappaport, S., & Fabrycky, D. 2011, *ApJ*, 728, 139  
 Chatterjee, S., Ford, E. B., Matsumura, S., & Rasio, F. A. 2008, *ApJ*, 686, 580  
 Deming, D., Knutson, H., Kammer, J., et al. 2015, *The Astrophysical Journal*, 805, 132  
 Eastman, J., Siverd, R., & Gaudi, B. S. 2010, *PASP*, 122, 935  
 Esteves, L. J., De Mooij, E. J. W., & Jayawardhana, R. 2015, *ApJ*, 804, 150  
 Fabrycky, D., & Tremaine, S. 2007, *ApJ*, 669, 1298  
 Foreman-Mackey, D., Hogg, D. W., Lang, D., & Goodman, J. 2013, *PASP*, 125, 306



TABLE 1  
SYSTEM PARAMETERS OF QATAR-2A

Parameter		Ref.
Stellar Parameters		
$T_{\text{eff}}$ (K)	$4645 \pm 50$	A
$\log g$ (dex)	$4.601 \pm 0.018$	A
[Fe/H] (dex)	$-0.02 \pm 0.08$	B
$v \sin i_*$ (km s $^{-1}$ )	$2.8 \pm 0.5$	A
$M_*$ ( $M_{\odot}$ )	$0.74 \pm 0.037$	A
$R_*$ ( $R_{\odot}$ )	$0.713 \pm 0.018$	A
Apparent V mag	13.3	A
$P_{\text{rot}}$ (days)	$18.5 \pm 1.9$	C
Age (Gyrochronology, Gyr)	$1.4 \pm 0.3$	C
Age (Isochrone, Gyr)	$15.72 \pm 1.36$	B
$u_1$	$0.6231 \pm 0.0057$	C
$u_2$	$0.062 \pm 0.015$	C
Planetary Parameters		
$P$ (days)	$1.337116553 \pm 0.000000044$	C
$T_c$ (BJD)	$2455617.581506 \pm 0.000054$	C
$R_*/a$	$0.15350 \pm 0.00018$	C
$a$ (AU)	$0.02160 \pm 0.00057$	C
$R_p/R_*$	$0.16208 \pm 0.00018$	C
$R_p$ ( $R_{\text{Jup}}$ )	$1.150 \pm 0.030$	C
$i$ ( $^{\circ}$ )	$89.7 \pm 0.5$	C
$b$	$0.03 \pm 0.06$	C
$M_{p,\text{RV}}$ ( $M_{\text{Jup}}$ )	$2.487 \pm 0.086$	A
$M_{p,\text{ELV}}$ ( $M_{\text{Jup}}$ )	$2.6 \pm 0.9$	C
$M_{p,\text{DB}}$ ( $M_{\text{Jup}}$ )	$3.9 \pm 1.5$	C
$e$ (assumed)	0	A

NOTE. — A: Bryan et al. (2012); B: Maxted et al. (2015); C: this work.

Gandolfi, D., Parviainen, H., Fridlund, M., et al. 2013, A&A, 557, A74  
 Gaudi, B. S., & Winn, J. N. 2007, ApJ, 655, 550  
 Howell, S. B., Sobeck, C., Haas, M., et al. 2014, PASP, 126, 398  
 Kipping, D. M., & Spiegel, D. S. 2011, MNRAS, 417, L88  
 Kreidberg, L. 2015, PASP, 127, 1161  
 Levrard, B., Winisdoerffer, C., & Chabrier, G. 2009, ApJ, 692, L9  
 Lin, D. N. C., Bodenheimer, P., & Richardson, D. C. 1996, Nature, 380, 606  
 Lomb, N. R. 1976, Astrophysics and Space Science, 39, 447  
 Luger, R., Agol, E., Kruse, E., et al. 2016, ArXiv e-prints, arXiv:1607.00524  
 Mancini, L., Southworth, J., Ciceri, S., et al. 2014, MNRAS, 443, 2391  
 —. 2016, MNRAS, 462, 4266  
 Maxted, P. F. L., Serenelli, A. M., & Southworth, J. 2015, A&A, 577, A90  
 Mazeh, T., & Faigler, S. 2010, A&A, 521, L59  
 Močnik, T., Southworth, J., & Hellier, C. 2016, ArXiv e-prints, arXiv:1608.07524

Newville, M., Stensitzki, T., Allen, D. B., & Ingargiola, A. 2014, LMFIT: Non-Linear Least-Square Minimization and Curve-Fitting for Python, doi:10.5281/zenodo.11813  
 Nutzman, P. A., Fabrycky, D. C., & Fortney, J. J. 2011, ApJ, 740, L10  
 Ohta, Y., Taruya, A., & Suto, Y. 2005, ApJ, 622, 1118  
 Pope, B. J. S., Parviainen, H., & Aigrain, S. 2016, MNRAS, arXiv:1606.01264  
 Queloz, D., Mayor, M., Weber, L., et al. 2000, A&A, 354, 99  
 Sanchis-Ojeda, R., & Winn, J. N. 2011, ApJ, 743, 61  
 Sanchis-Ojeda, R., Winn, J. N., Holman, M. J., et al. 2011, ApJ, 733, 127  
 Scargle, J. D. 1982, ApJ, 263, 835  
 Schlaufman, K. C. 2010, ApJ, 719, 602  
 Silva, A. V. R. 2003, ApJ, 585, L147  
 Silva-Valio, A., Lanza, A. F., Alonso, R., & Barge, P. 2010, A&A, 510, A25  
 Vanderburg, A., & Johnson, J. A. 2014, PASP, 126, 948  
 Vanderburg, A., Latham, D. W., Buchhave, L. A., et al. 2016, ApJS, 222, 14  
 Winn, J. N., Fabrycky, D., Albrecht, S., & Johnson, J. A. 2010, ApJ, 718, L145

TABLE 2  
MID-TRANSIT TIMES OF QATAR-2B

Epoch	$T_c$ (BJD - 2454900)	Unc.	Ref.
-1197	717.58156	0.00082	1
-1192	724.26679	0.00011	2
-1141	792.46109	0.00270	1
-1135	800.47915	0.00083	1
-930	1074.59334	0.00072	3
-927	1078.6048	0.0012	4
-921	1086.62711	0.00069	5
-894	1122.72850	0.00018	6
-894	1122.72800	0.00017	7
-894	1122.72815	0.00016	8
-894	1122.72810	0.00022	9
-891	1126.73842	0.00033	10
-888	1130.7516	0.0015	11
-885	1134.76157	0.00010	6
-885	1134.76196	0.00012	7
-885	1134.76198	0.00015	8
-885	1134.76249	0.00015	9
-883	1137.43785	0.00068	12
-882	1138.77329	0.00010	7
-882	1138.77345	0.00012	8
-882	1138.77312	0.00015	9
-877	1145.45890	0.00042	13
-868	1157.49242	0.00018	14
-868	1157.49246	0.00028	15
-868	1157.49274	0.00016	16
-868	1157.49282	0.00023	17
-659	1436.94926	0.00059	18
-657	1439.62434	0.00027	19
-654	1443.6346	0.0011	20
-616	1494.44559	0.00056	21
-604	1510.4905	0.0010	22
-603	1511.8302	0.00058	23
-597	1519.8502	0.0013	24
-580	1542.58191	0.00014	25
0	2318.109992	0.000049	26
1	2319.447169	0.000049	26
2	2320.784315	0.000050	26
3	2322.121328	0.000049	26
4	2323.458458	0.000051	26
5	2324.795643	0.000049	26
6	2326.132714	0.000090	26
7	2327.469972	0.000050	26
8	2328.807039	0.000057	26
9	2330.143911	0.000099	26
10	2331.481166	0.000050	26

NOTE. — References: (1) Canis Major Observatory (Mancini et al. 2014); (2) Bryan et al. (2012); (3) Strajnic et al. (TRESCA); (4) Zibar M. (TRESCA); (5) Gonzales J. (TRESCA); (6) MPG/ESO 2.2m  $g'$  (Mancini et al. 2014); (7) MPG/ESO 2.2m  $r'$  (Mancini et al. 2014); (8) MPG/ESO 2.2m  $i'$  (Mancini et al. 2014); (9) MPG/ESO 2.2m  $z'$  (Mancini et al. 2014); (10) Dax T. (TRESCA); (11) Masek M. (TRESCA); (12) Carreno A. (TRESCA); (13) Montigiani N., Manucci M. (TRESCA); (14) Cassini 1.52m (Mancini et al. 2014); (15) CAHA 2.2m  $g$  (Mancini et al. 2014); (16) CAHA 2.2m  $r$  (Mancini et al. 2014); (17) CAHA 2.2m  $z$  (Mancini et al. 2014); (18) Campbell J. (TRESCA); (19) CAHA 1.23m (Mancini et al. 2014); (20) Ren'e R. (TRESCA); (21) Ayiomamitis A. (TRESCA); (22) Jacobsen J. (TRESCA); (23) Kehusmaa P., Harlinton C. (TRESCA); (24) Shadic S. (TRESCA); (25) Colazo C., et al. (TRESCA); (26) K2 (this work). TRESCA stands for "TRansiting ExoplanetS and CAandidates".

TABLE 3  
TABLE. 2 CONTINUED

11	2332.818338	0.000052	26
12	2334.155345	0.000059	26
13	2335.492644	0.000079	26
14	2336.829644	0.000096	26
15	2338.166710	0.000060	26
16	2339.503878	0.000056	26
17	2340.840863	0.000056	26
18	2342.177965	0.000071	26
19	2343.515114	0.000049	26
20	2344.852294	0.000055	26
21	2346.189436	0.000068	26
22	2347.526675	0.000090	26
23	2348.863781	0.000075	26
24	2350.200849	0.000049	26
25	2351.537860	0.000052	26
26	2352.875083	0.000068	26
27	2354.212212	0.000052	26
28	2355.549382	0.000053	26
29	2356.886369	0.000052	26
30	2358.223494	0.000054	26
31	2359.560744	0.000049	26
32	2360.897787	0.000059	26
33	2362.234890	0.000054	26
34	2363.572009	0.000055	26
35	2364.909290	0.000106	26
36	2366.246114	0.000051	26
37	2367.583411	0.000049	26
38	2368.920242	0.000078	26
39	2370.257464	0.000054	26
40	2371.594669	0.000056	26
41	2372.931863	0.000048	26
42	2374.269011	0.000055	26
43	2375.605990	0.000056	26
44	2376.943205	0.000051	26
45	2378.280327	0.000069	26
46	2379.617357	0.000051	26
47	2380.954439	0.000054	26
48	2382.291665	0.000071	26
49	2383.628818	0.000079	26
50	2384.965898	0.000053	26
51	2386.302902	0.000052	26
52	2387.640011	0.000091	26
53	2388.977140	0.000051	26
54	2390.314349	0.000050	26
55	2391.651335	0.000051	26
56	2392.988456	0.000058	26
57	2394.325632	0.000048	26
58	2395.662874	0.000052	26

TABLE 4  
SPOT-CROSSING ANOMALIES OBSERVED IN K2

Epoch	$t_{\text{anom}}$ (BJD - 2454900)	Amplitude	Width (days)	No.
6	2326.12087 ± 0.00097	0.00112 ± 0.00019	0.00503 ± 0.00123	1
18	2342.15048 ± 0.00126	0.00092 ± 0.00023	0.00416 ± 0.00086	1
19	2343.49928 ± 0.00059	0.00154 ± 0.00021	0.00336 ± 0.00049	1
21	2346.20227 ± 0.00078	0.00164 ± 0.00037	0.00597 ± 0.00158	1
22	2347.55201 ± 0.00096	0.00105 ± 0.00030	0.00307 ± 0.00099	1
32	2360.87726 ± 0.00041	0.00195 ± 0.00025	0.00296 ± 0.00048	1
33	2362.22691 ± 0.00043	0.00213 ± 0.00020	0.00387 ± 0.00043	1
34	2363.57898 ± 0.00027	0.00316 ± 0.00021	0.00361 ± 0.00033	1
35	2364.92923 ± 0.00118	0.00192 ± 0.00034	0.00808 ± 0.00187	1
45	2378.25545 ± 0.00075	0.00185 ± 0.00019	0.00523 ± 0.00072	1
46	2379.60347 ± 0.00042	0.00252 ± 0.00019	0.00468 ± 0.00045	1
47	2380.95384 ± 0.00035	0.00299 ± 0.00019	0.00484 ± 0.00038	1
48	2382.30534 ± 0.03138	0.00262 ± 0.00029	0.00429 ± 0.00066	1
49	2383.65482 ± 0.00065	0.00180 ± 0.00032	0.00405 ± 0.00078	1
9	2330.13165 ± 0.00169	0.00152 ± 0.00028	0.01160 ± 0.00234	2
10	2331.48471 ± 0.00084	0.00174 ± 0.00021	0.00739 ± 0.00137	2
11	2332.83334 ± 0.02299	0.00095 ± 0.00045	0.00607 ± 0.00289	2
12	2334.18152 ± 0.00097	0.00092 ± 0.00046	0.00243 ± 0.00152	2
21	2346.16120 ± 0.00175	0.00095 ± 0.00041	0.00494 ± 0.00154	2
22	2347.50724 ± 0.00076	0.00198 ± 0.00027	0.00682 ± 0.00096	2
23	2348.85870 ± 0.00098	0.00318 ± 0.00089	0.00958 ± 0.00205	2
24	2350.20992 ± 0.00094	0.00200 ± 0.00021	0.00695 ± 0.00105	2
25	2351.55931 ± 0.00055	0.00137 ± 0.00026	0.00261 ± 0.00073	2
35	2364.88900 ± 0.00115	0.00187 ± 0.00035	0.00577 ± 0.00195	2
36	2366.23833 ± 0.00067	0.00184 ± 0.00021	0.00459 ± 0.00069	2
37	2367.58754 ± 0.00086	0.00145 ± 0.00018	0.00663 ± 0.00085	2
49	2383.61220 ± 0.00081	0.00156 ± 0.00031	0.00514 ± 0.00129	2
50	2384.96188 ± 0.00042	0.00249 ± 0.00018	0.00534 ± 0.00039	2
51	2386.31324 ± 0.00068	0.00166 ± 0.00019	0.00585 ± 0.00067	2
52	2387.66170 ± 0.00065	0.00144 ± 0.00022	0.00356 ± 0.00075	2
10	2331.46583 ± 0.00055	0.00208 ± 0.00022	0.00413 ± 0.00059	3
11	2332.81711 ± 0.00039	0.00258 ± 0.00038	0.00304 ± 0.00040	3
12	2334.16835 ± 0.00039	0.00244 ± 0.00023	0.00380 ± 0.00040	3
13	2335.52029 ± 0.00088	0.00127 ± 0.00028	0.00332 ± 0.00084	3
23	2348.84053 ± 0.00135	0.00138 ± 0.00036	0.00499 ± 0.00162	3
24	2350.19119 ± 0.00100	0.00160 ± 0.00022	0.00504 ± 0.00123	3
25	2351.54429 ± 0.00045	0.00193 ± 0.00022	0.00368 ± 0.00053	3
26	2352.89844 ± 0.00168	0.00092 ± 0.00019	0.00602 ± 0.00187	3
12	2334.15237 ± 0.00053	0.00138 ± 0.00026	0.00273 ± 0.00055	4
13	2335.50433 ± 0.00071	0.00113 ± 0.00040	0.00199 ± 0.00289	4
21	2346.18160 ± 0.00095	0.00109 ± 0.00040	0.00358 ± 0.00136	5
22	2347.53394 ± 0.00141	0.00076 ± 0.00041	0.00281 ± 0.00397	5
23	2348.88640 ± 0.00076	0.00166 ± 0.00051	0.00346 ± 0.00100	5
35	2364.90513 ± 0.00032	0.00217 ± 0.00033	0.00189 ± 0.00060	5
49	2383.63367 ± 0.00098	0.00099 ± 0.00036	0.00395 ± 0.00168	5
52	2387.62708 ± 0.00040	0.00180 ± 0.00026	0.00254 ± 0.00039	6
53	2388.97723 ± 0.00098	0.00147 ± 0.00023	0.00952 ± 0.00237	6
54	2390.33064 ± 0.00092	0.00105 ± 0.00023	0.00350 ± 0.00091	6

TABLE 5  
RESULTS OF THE GEOMETRIC MODEL

Parameter	Spot 1	Spot 2	Spot 3	Combined
$\lambda$ ( $^{\circ}$ )	0.0 ± 4.4	0.0 ± 4.4	0.0 ± 6.3	0.0 ± 2.8
$i_s$ ( $^{\circ}$ )	90 ± 22	90 ± 22	90 ± 24	90 ± 19
$l$ ( $^{\circ}$ )	1 ± 18	2 ± 19	1 ± 21	2 ± 16
$P_{\text{rot}}$ (days)	17.89 ± 0.14	17.98 ± 0.15	17.99 ± 0.50	17.94 ± 0.10

TABLE 6  
RESULTS OF THE NUMERICAL MODELS

Parameter	Spot rod	Pixelated Model
$\lambda$ ( $^{\circ}$ )	$1.4^{+3.0}_{-1.7}$	$4.3^{+4.6}_{-2.7}$
$i_s$ ( $^{\circ}$ )	$89.8 \pm 4.0$	$90.1 \pm 7.9$
$l$ ( $^{\circ}$ )	$6.2^{+7.3}_{-4.2}$	$5.4^{+7.5}_{-6.8}$
$P_{\text{rot}}$ (days)	$18.62 \pm 0.31$	$18.54 \pm 0.40$
$t_{\text{anom}}$ (BJD - 2454900)	$2380.953 \pm 0.025$	$2380.928 \pm 0.025$
$\alpha$ ( $^{\circ}$ )	$11.2 \pm 1.2$	$12.7 \pm 0.7$
$f$	$0.90 \pm 0.02$	$0.92 \pm 0.01$